Extended Data

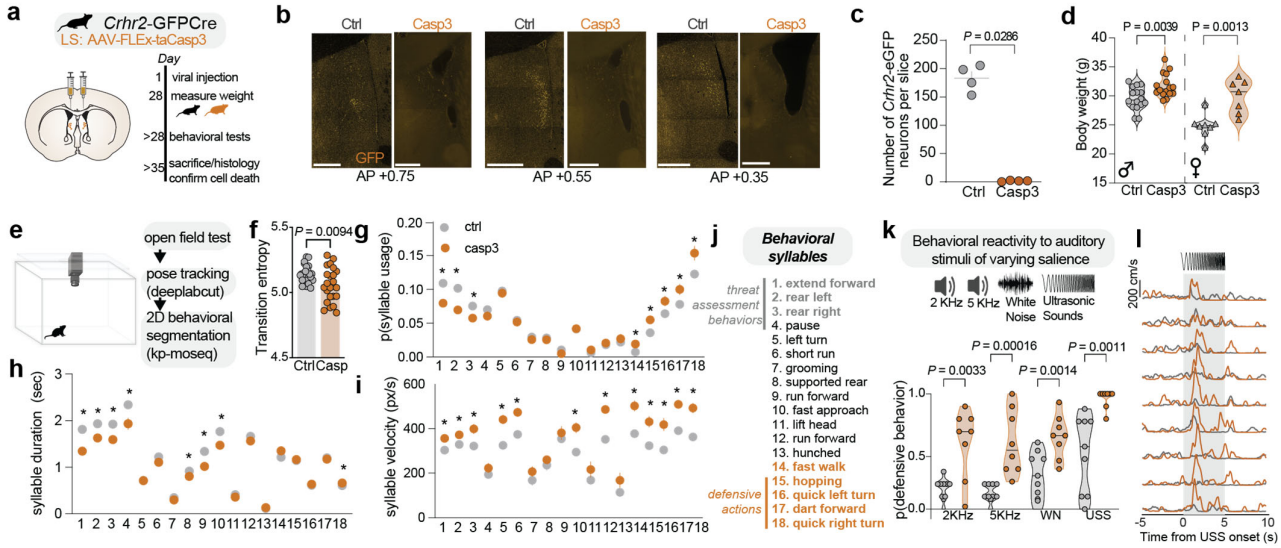

Extended Data Figure 1: Genetic ablation of LS *Crhr2* neurons alters behavioral responsivity to environmental stimuli. **a**, Experimental timeline and schematic for selective ablation of LS^{Crhr2} neurons via Cre-dependent expression of Caspase-3. **b**, Representative images confirming Caspase-3-induced neuronal ablation compared to control (Ctrl); GFP expression (in orange) marks *Crhr2* neurons. Scale bars, 500um. **c**, Quantification showing significant reduction in GFP-positive Crhr2 neurons following Caspase-3 treatment (n= 3 slices per mouse, 4 mice/group, two-tailed t-test, ***P*** = 0.0286). **d**, Violin plots depicting significant reduction in body weight 4 weeks post-ablation in Casp3-treated mice compared to Ctrl groups in both males and female mice (two-tailed t-tests, male : n=16 ctrl, 16 Casp3, *P* =0.0039, female: n=8 ctrl, 7 Casp3, *P* =0.0013). **e**, Schematic illustrating open field test with 2D behavioral segmentation using deep-learning-based tracking (DeepLabCut) and keypoint-moseq (kp-moseq). **f**, Behavioral transition entropy is reduced in Casp3 mice compared to Ctrl indicating that *Crhr2* neuron ablation induces more predictable syllable transitions (n=24 Ctrl, 23 Casp3, two-tailed t-test, *P* = 0.0094). **g–i**, Comparisons of behavioral syllable usage (**g**), duration (**h**), and velocity (**i**) between Ctrl and Casp3 mice (n=24 Ctrl, 23 Casp3, two-way ANOVAs and post-hoc Bonferonni's multiple comparison tests; duration: *P*<0.0001 interaction, *P*<0.0001 syllable; p(syllable usage), *P*<0.0001 interaction, *P*<0.0001 syllable; velocity: *P*<0.0001 interaction, *P*<0.0001 syllable). **j**, List of identified behavioral syllables categorized into threat assessment and defensive behaviors. Casp3 mice reduce threat assessment behaviors while increasing defensive behaviors, suggesting a dysregulation in the ability to evaluate environmental stimuli. **k**, Behavioral reactivity (i.e. defensive behaviors) to auditory stimuli of varying salience, showing significantly increased reactivity in Casp3-treated mice (n=9 Ctrl, 8 Casp3, Multiple Mann-Whitney tests; white noise: *P* = 0.0033, 2 kHz tone: *P* = 0.00016, 5 kHz tone: *P* = 0.0014, and ultrasonic sound [USS]: *P* = 0.0011)). **l**, Mean velocity traces in response to repeated USS presentations (ascending from bottom to top) illustrating enhanced responsivity of Casp3-treated mice. Casp3 group is depicted in orange. Ctrl group is depicted in gray. *p<0.05.

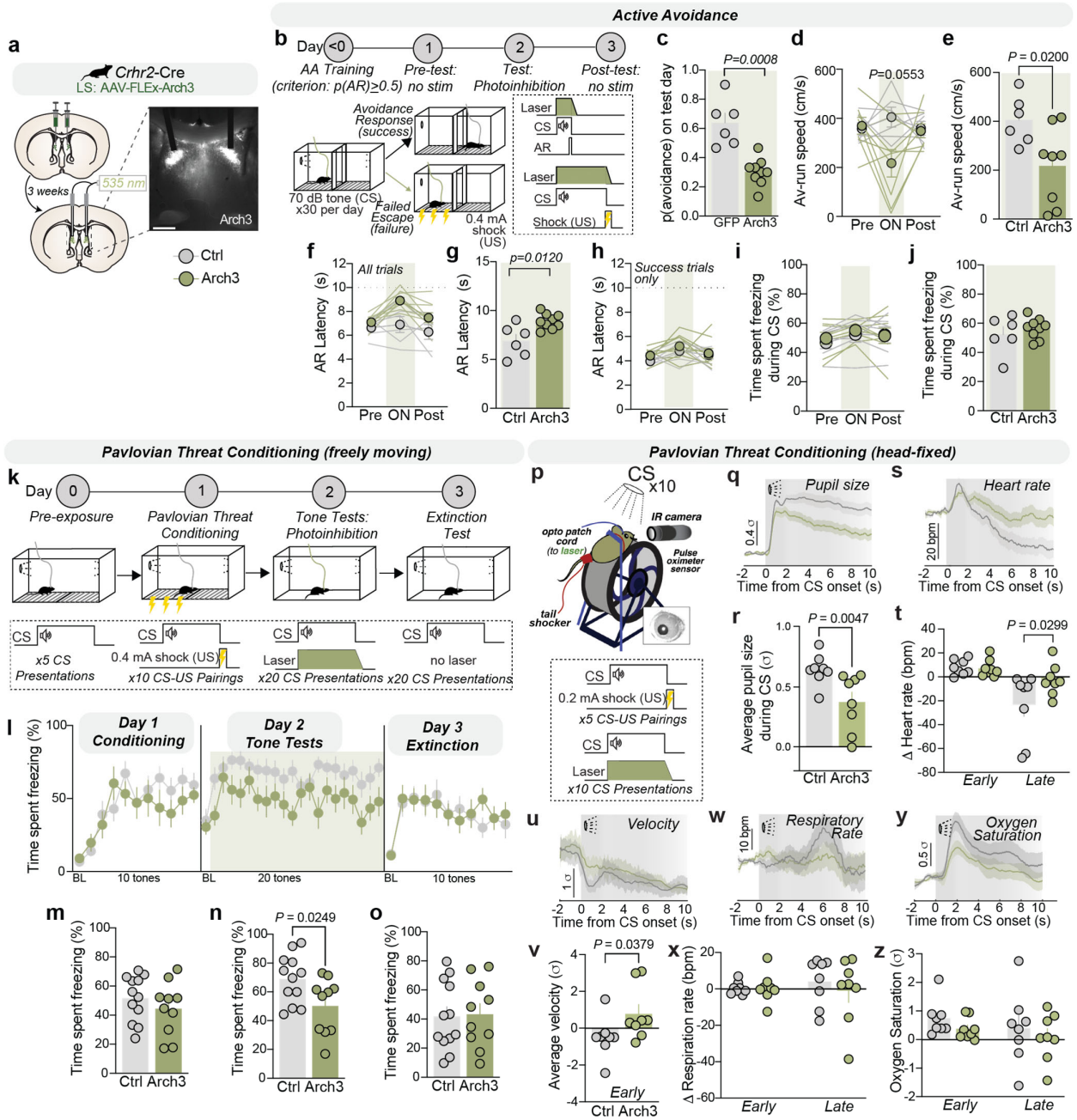
Active Avoidance
a
Crhr2-Cre
LS: AAV-FLEx-Arch3
3 weeks
535 nm
Arch3
Ctrl
Arch3
b
Day
AA Training
(criterion: p(AR)≥0.5)
Pre-test:
no stim
Test:
Photoinhibition
Post-test:
no stim
Avoidance
Response
(success)
70 dB tone (CS)
x30 per day
Failed
Escape
(failure)
0.4 mA
shock
(US)
Laser
CS
AR
Shock (US)
c
P=0.0008
p(avoidance) on test day
GFP Arch3
d
P=0.0553
Av-run speed (cm/s)
Pre ON Post
e
P = 0.0200
Av-run speed (cm/s)
Ctrl Arch3
f
All trials
AR Latency (s)
Pre ON Post
g
p=0.0120
AR Latency (s)
Ctrl Arch3
h
Success trials
only
AR Latency (s)
Pre ON Post
i
Time spent freezing
during CS (%)
Pre ON Post
j
Time spent freezing
during CS (%)
Ctrl Arch3
Pavlovian Threat Conditioning (freely moving)
k
Day
Pre-exposure
Pavlovian Threat
Conditioning
Tone Tests:
Photoinhibition
Extinction
Test
CS
x5 CS
Presentations
0.4 mA shock (US)
x10 CS-US Pairings
Laser
x20 CS Presentations
no laser
x20 CS Presentations
l
Day 1
Conditioning
Day 2
Tone Tests
Day 3
Extinction
Time spent freezing (%)
BL
10 tones
BL
20 tones
BL
10 tones
m
Time spent freezing (%)
Ctrl Arch3
n
P = 0.0249
Time spent freezing (%)
Ctrl Arch3
o
Time spent freezing (%)
Ctrl Arch3
Pavlovian Threat Conditioning (head-fixed)
p
CS
x10
IR camera
opto patch
cord
(to laser)
Pulse
oximeter
sensor
tail
shocker
CS
0.2 mA shock (US)
x5 CS-US Pairings
CS
Laser
x10 CS Presentations
q
Pupil size
0.4 σ
Time from CS onset (s)
s
Heart rate
20 bpm
Time from CS onset (s)
r
P = 0.0047
Average pupil size
during CS (σ)
Ctrl Arch3
t
P = 0.0299
Δ Heart rate (bpm)
Early
Late
u
Velocity
1 σ
Time from CS onset (s)
w
Respiratory
Rate
10 bpm
Time from CS onset (s)
y
Oxygen
Saturation
0.5 σ
Time from CS onset (s)
v
P = 0.0379
Average velocity (σ)
Early
Ctrl Arch3
x
Δ Respiration rate (bpm)
Early
Late
z
Oxygen Saturation (σ)
Early
Late

Extended Data Figure 2: Photoinhibition of the LS *Crhr2* population suppresses adaptive behavioral and physiological threat responses. **a**, Schematic illustrating the viral strategy and expression of Arch3 for optogenetic inhibition in LS^{Crhr2} neurons; representative expression shown. Scale bar, 500um. **b**, Timeline and schematic of active avoidance (AA) experimental design, including photoinhibition period during the CS in success and failure trials. **c–j**, Behavioral analyses during active avoidance tasks: (**c**) LS^{Crhr2} photoinhibition suppressed avoidance on test day (two-tailed t-test, *P*=0.0008, n=6 GFP, 9 Arch3), (**d–e**) reduced avoidance vigor (**d**: n = 6 GFP, 9 Arch3; repeated measure two-way ANOVA, *P*=0.0237; Bonferroni multiple comparisons post-hoc tests, *P*= 0.0553; **e**: two-tailed t-test, *P*=0.0200), (**f–g**) increased avoidance run (Av-run) latency when accounting for all trials (n=6 GFP, 9 Arch3**, f**: repeated measure two-way ANOVA, *P*=0.0122; Bonferroni multiple comparisons post-hoc tests, *P*= 0.0804; **g**: two-tailed t-test, *P*=0.0120), (**h**) did not change avoidance run (Av-run) latency only during success trials (two-way repeated measures ANOVA, *P*=0.0871), (**i**) did not change time spent freezing during the CS before, during, and after the day of photoinhibition (two-way repeated measures ANOVA, *P*=0.6896) or (**j**) during the CS on the test day (two-tailed t-tests, *P*=0.4426). **k**, Experimental design for Pavlovian threat conditioning (inescapable threat) in freely moving mice. **l**, Average time spent freezing during the CS tone presentations across conditioning, tone test, and extinction days. Photoinhibition occurred during the CS only on the tone test day trials. LS^{Crhr2} photoinhibition markedly reduced freezing during the tone tests in the inescapable pavlovian threat conditioning paradigm. Circles represent single trials (mean ± SEM) , n=12 Ctrl, 10 GFP. **m–o**, Average freezing behavior across all trials per day: (**m**) conditioning day (two-tailed t-test, P=0.3281), (**n**) tone test day (two-tailed t-test, *P*=0.0249), (**o**) extinction day (two-tailed t-test, *P*=0.8746) **p**, Schematic for the experimental setup and design for Pavlovian threat conditioning in head-fixed mice, allowing simultaneous recording of physiological metrics. **q–z**, Physiological measures aligned to CS presentations during photoinhibition test day: (**q–r**) Normalized pupil size during CS; LS^{Crhr2} photoinhibition attenuates CS-evoked pupil dilation; (**q**) average pupil size trace, dark line mean ± SEM, scale bar 0.4 SD from mean; (**r**) average pupil size during CS (n=8/group, two-tailed t-test, *P*=0.0047; (**s–t**) Normalized heart rate responses during CS; LS^{Crhr2} photoinhibition attenuates CS-evoked heart rate fluctuations; (**s**) mean heart rate trace aligned to CS onset, shaded SEM; (**t**) average heart rate changes during early and late CS periods (repeated measure two-way ANOVA, *P*=0.0943; Bonferonni multiple comparisons post-hoc tests, early [0-2 seconds]: *P*=0.9945, late [8-10 seconds]: *P*=0.0299). (**u–v**) Average velocity aligned to CS onset; (**u**) average trace ± SEM; (**v**) mean velocity during early CS period (early, 0-2 seconds), two-tailed t-test, P=0.0379. (**w–x**) Respiratory rate responses aligned to CS; (**w**) mean respiratory trace ± SEM (shaded); (**x**) average respiratory rate (repeated measure two-way ANOVA, *P*=0.4450; Bonferonni multiple comparisons post-hoc tests, early [0-2 seconds]: *P*=0.9983, late [8-10 seconds]: *P*=0.6522). (**y–z**) Oxygen saturation levels aligned to CS; (**y**) average trace ± SEM; (**z**) average oxygen saturation (repeated measure two-way ANOVA, *P*=0.8791; Bonferonni multiple comparisons post-hoc tests, early [0-2 seconds]: *P*=0.6129, late [8-10 seconds]: *P*=0.7015). Green = Arch3 group. Gray = Control (Ctrl) group.

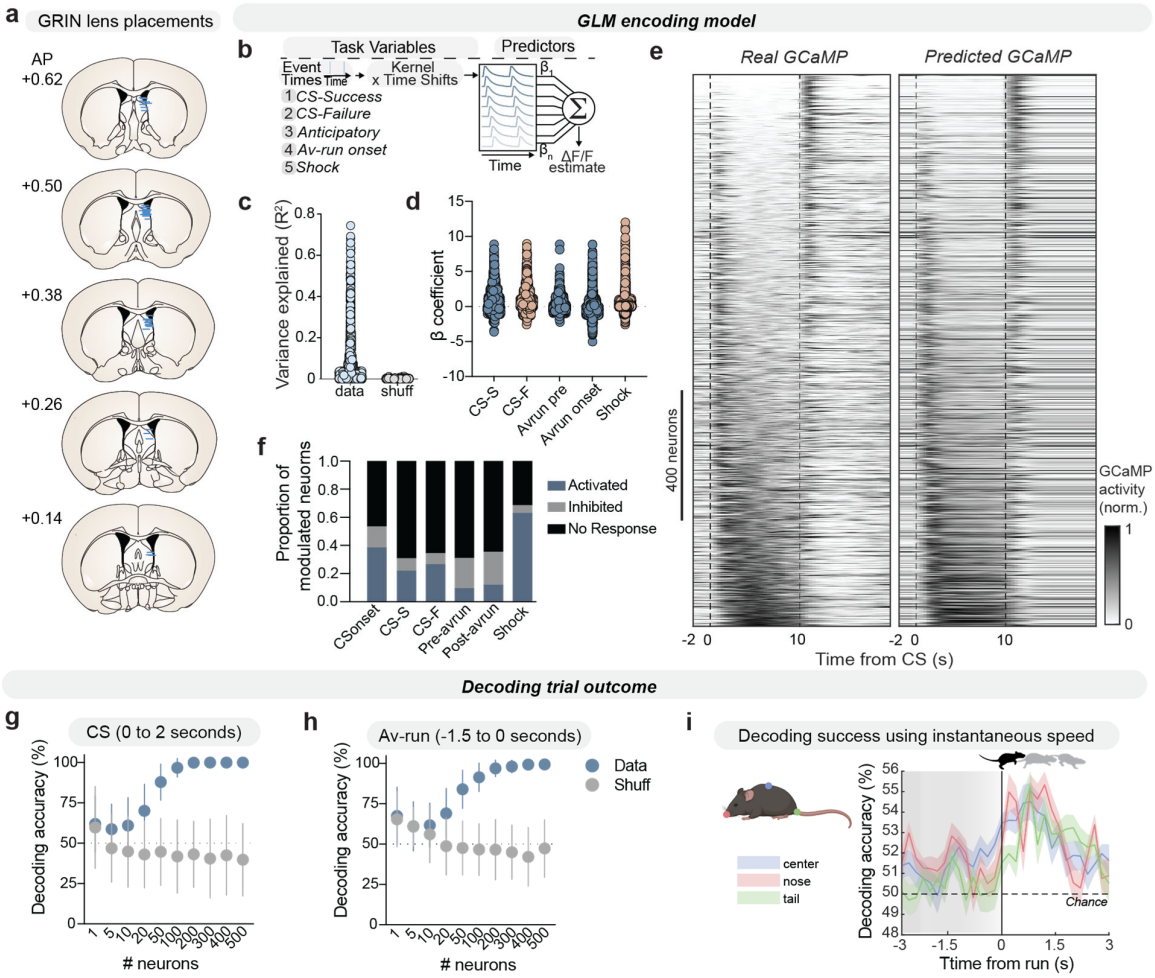

Extended Data Figure 3: Characterization of LS *Crhr2* population dynamics during active avoidance. **a**, Anatomical placements of gradient index (GRIN) lenses for microendoscopic calcium imaging across the anterior-posterior (AP) axis of LS. **b**, Schematic of generalized linear model (GLM) used to predict neural activity from key task variables (CS success/failure, anticipatory Av-run, Av-run onset, shock). **c**, Variance explained (R^2) for real vs. shuffled data, indicating significant encoding of task variables by LS^{Crhr2} neurons (two-tailed t-test, $P<0.0001$). **d**, GLM β coefficients showing the strength and directionality of neuronal modulation by each task variable across neurons. **e**, Heatmaps comparing average real and GLM-predicted GCaMP signals aligned to CS onset across neurons, illustrating model fit accuracy. **f**, Proportion of neurons activated, inhibited, or showing no response across task events (CS onset, success/failure, anticipatory Av-run, Av-run onset, shock) according to AUROC analysis. **g–h**, Decoding accuracy (linear SVM classifier) predicting trial outcomes using neuronal activity aligned to (**g**) CS onset (0–2 sec) and (**h**) anticipatory Av-run (-1.5–0 sec) using different sample numbers of random neurons as the training set, demonstrating increased predictive capacity compared to shuffled controls with higher number of neurons. **i**, Decoding accuracy for Av-run initiation using instantaneous speed from different body parts (center, nose, tail), illustrating lack of predictive ability preceding the Av-run using running speed itself.

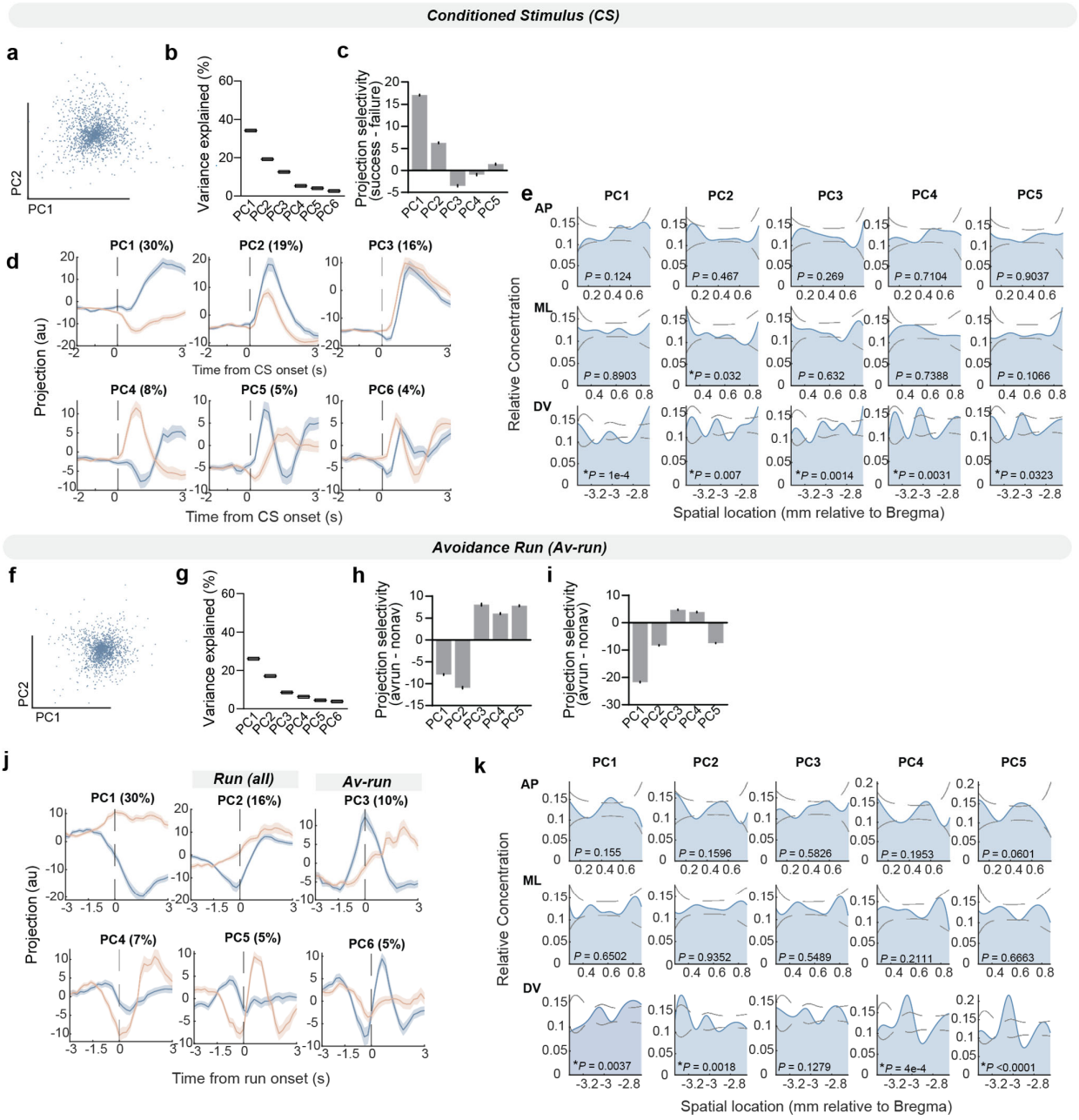

Extended Data Figure 4: Principal component analysis reveals spatially organized representations of threat-related features at CS onset and avoidance-run. **a**, Principal component analysis (PCA) scatterplot illustrating neuronal population activity patterns aligned to conditioned stimulus (CS) onset. **b**, Variance explained by each principal component (PC) for CS-aligned neuronal activity. **c**, Selectivity of neural activity projection onto principal components comparing successful vs. failed avoidance trials (mean ± SEM), illustrating projection selectivity towards success for PC1 and PC2, and toward failure for PC3. **d**, CS-aligned neural activity projections onto the top six PCs, indicating distinct temporal dynamics and selectivity for success (blue) or failure (orange) trials. **e**, Spatial distribution plots showing relative anatomical concentration of neuronal contributions to each principal component across the anterior-posterior (AP), mediolateral (ML), and dorsoventral (DV) axes. **f–k**, Corresponding PCA analysis for neuronal activity aligned to avoidance-run (Av-run) onset, including (**f**) scatterplot, (**g**) variance explained by PCs, (**h–i**) projection selectivity, (**j**) PC temporal dynamics, and (**k**) anatomical distribution across spatial axes.

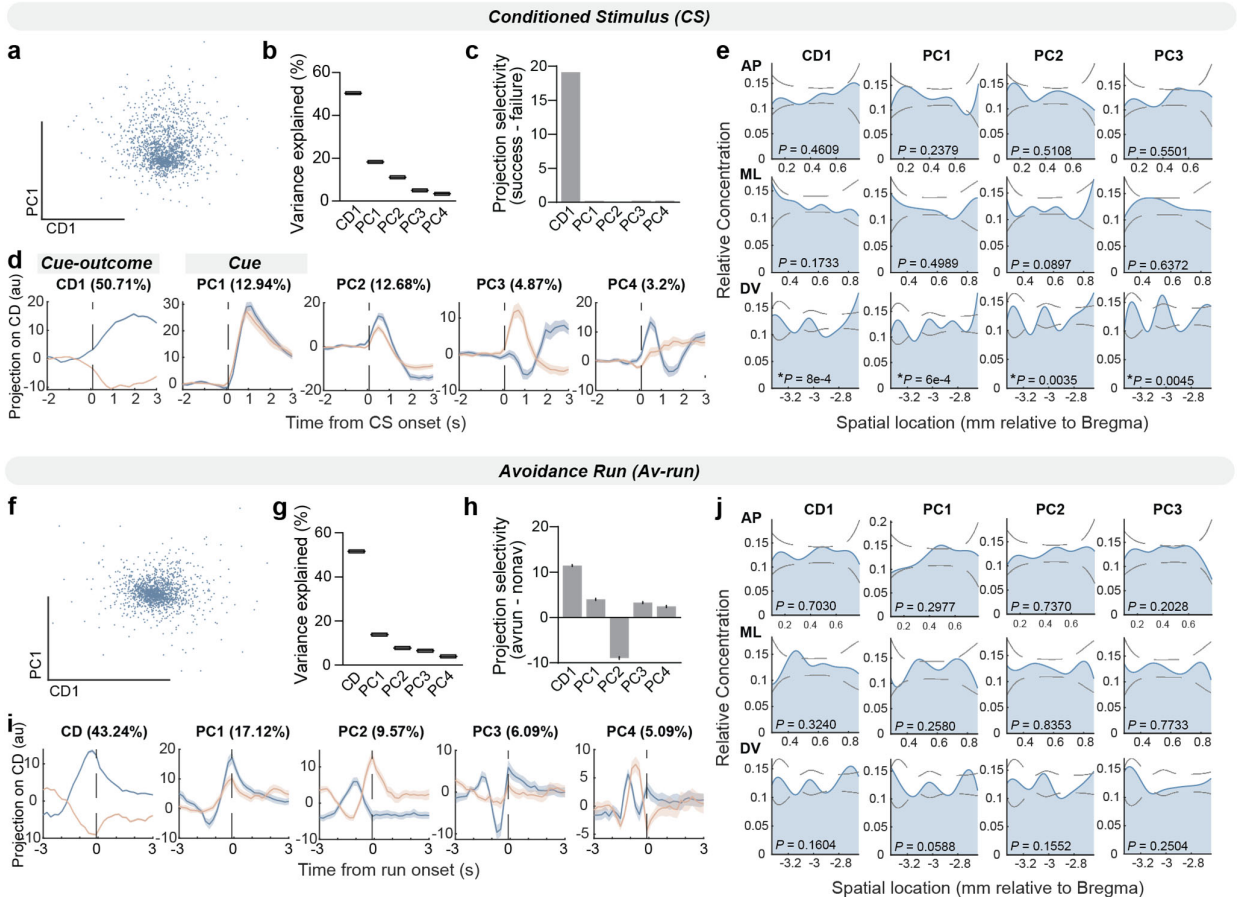

Extended Data Figure 5: Coding direction and principal component analysis delineate distinct neural dynamics and reveal spatially organized features related to threat processing. **a**, Scatterplot illustrating coding direction (CD) and PC1 of neuronal activity aligned to CS onset, distinguishing success from failure trials. **b**, Variance explained by CD and orthogonal PCs for CS-aligned neuronal activity. **c**, Projection selectivity quantifying differential neural responses for success vs. failure trials. **d**, Temporal activity profiles of CD and top PCs during CS onset, highlighting distinct selectivity for trial outcomes. **e**, Spatial distribution maps showing relative anatomical concentration along AP, ML, and DV axes for CD and principal components during CS epochs. **f–j**, Equivalent analyses for Av-run-aligned neuronal activity, including (**f**) scatterplot of CD and PC1, (**g**) variance explained, (**h**) selectivity of projections, (**i**) temporal dynamics, and (**j**) spatial distribution

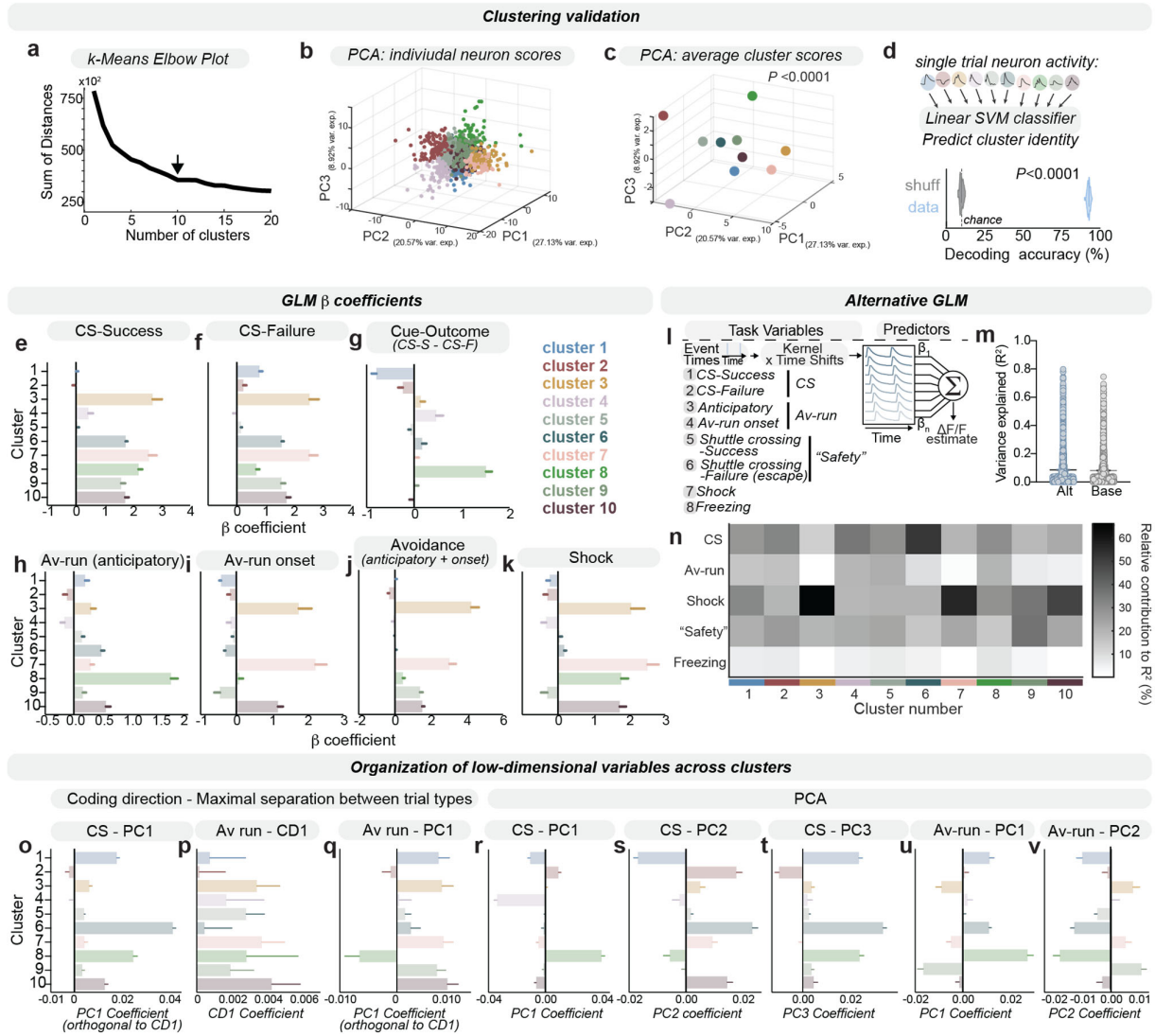

Extended Data Figure 6: Validation and characterization of functional clustering of the LS *Crhr2* population. **a**, Elbow plot for k-means clustering showing optimal cluster number selection (arrow). **b**, 3D PCA scatter plot of individual PC scores for each neuron, color-coded by cluster. **c**, PCA of average PC scores for each cluster revealing significant separation among clusters (ANOVA, $P < 0.0001$). **d**, Decoding accuracy for predicting neuronal cluster identity from single-trial neuronal activity (linear SVM classifier; $P < 0.0001$). **e–k**, GLM β coefficients for task-related events across clusters: (**e**) CS-Success, (**f**) CS-Failure, (**g**) Cue-outcome variable (CS-S minus CS-F), (**h**) anticipatory Av-run, (**i**) Av-run onset, (**j**) combined avoidance (anticipatory + onset), and (**k**) shock. **l–m**, Alternative GLM model incorporating additional task variables (schematic shown in **l**) with (**m**) variance explained (R^2) comparison against base GLM (**e-k**). **n**, Heatmap displaying relative contribution of task variables (CS, Av-run, shock, safety, freezing) to activity across clusters. **o–v**, Organization of coding direction (CD) and principal component analysis (PCA) variables across clusters highlighting differential functional specializations.

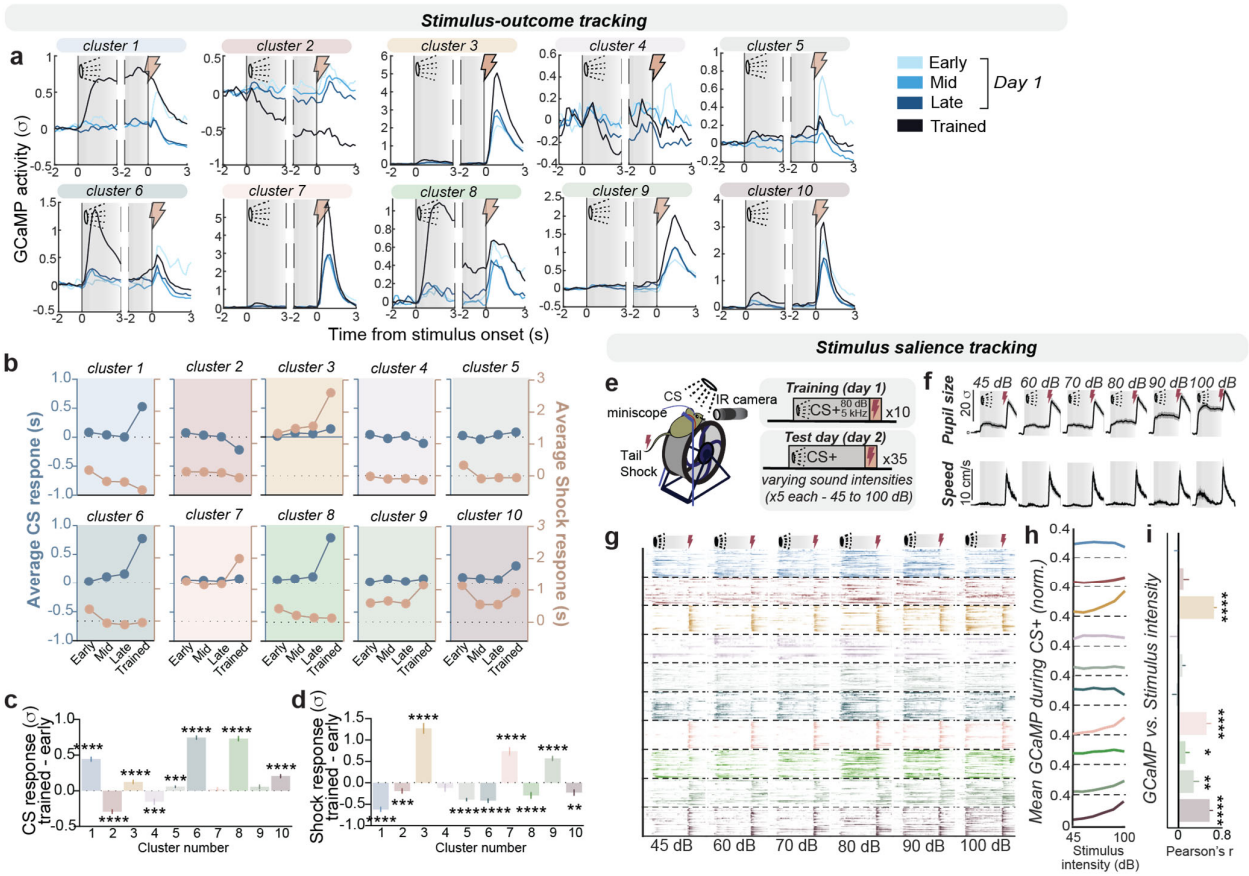

Extended Data Figure 7: Functional neuronal clusters differentially encode stimulus-outcome and stimulus-salience features. **a**, Average calcium (GCaMP) activity profiles for each neuronal cluster (clusters 1–10), aligned to conditioned stimulus (CS) and shock onset across different stages of active avoidance training (early, mid, late, and trained). **b**, Temporal evolution of neuronal responses to CS (blue) and shock (orange) throughout training, indicating cluster-specific patterns in encoding stimulus-outcome associations. **c–d**, Quantification of changes in neuronal responsiveness from early to trained stages of learning: (**c**) significant differences in CS response and (**d**) shock response across clusters (One-sample *t*-tests). **e**, Experimental design schematic for testing stimulus salience using varying auditory CS intensities (45–100 dB) in head-fixed mice with simultaneous neural recording. **f**, Representative pupil dilation and speed traces showing increased physiological and behavioral responses with higher stimulus intensities. **g**, Heatmap of single-neuron calcium responses across clusters for different auditory intensities, illustrating cluster-specific stimulus intensity encoding. **h–i**, Mean normalized GCaMP activity during CS presentations (**h**) and correlation (Pearson's r) between neuronal activity and stimulus intensity (**i**), highlighting robust encoding of stimulus salience across clusters (One-sample *t*-tests). *P < 0.05, **P < 0.01, ***P < 0.001,****P < 0.0001.

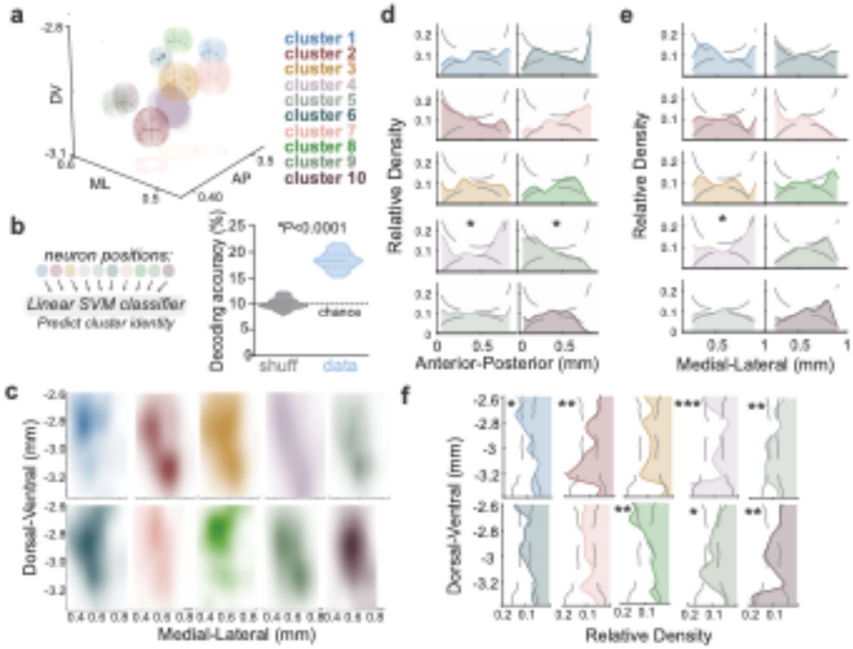

Extended Data Figure 8: Spatial organization of LS Crhr2 functional clusters. **a**, 3D (AP, ML, DV) spatial distribution map showing anatomical positioning of neuronal clusters within LS, color-coded by cluster identity. **b**, Linear SVM classifier accuracy for predicting cluster identity based on neuron spatial coordinates, demonstrating significant spatial clustering (unpaired two-tailed t-test, $P < 0.0001$). **c**, 2D relative density plots illustrating spatial distributions of clusters along medial-lateral (ML) and dorsal-ventral (DV) dimensions. **d–f**, Relative density distributions for each neuronal cluster across (**d**) anterior-posterior (AP), (**e**) medial-lateral (ML), and (**f**) dorsal-ventral (DV) axes, with significant differences indicated (permutation tests, see *Methods*). *$P < 0.05$, **P < 0.01, ***P < 0.001,****P < 0.0001.

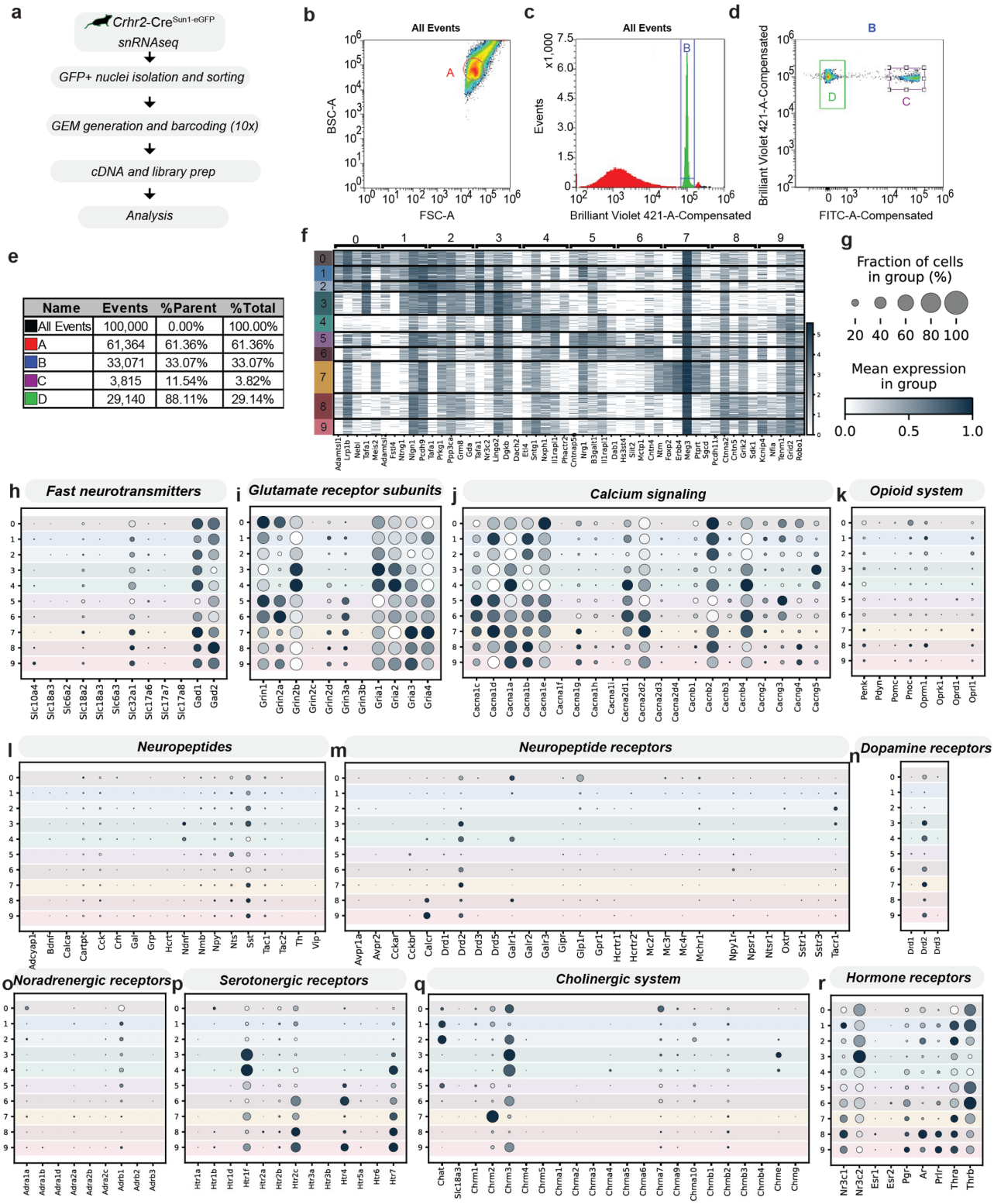

Name	Events	%Parent	%Total
All Events	100,000	0.00%	100.00%
A	61,364	61.36%	61.36%
B	33,071	33.07%	33.07%
C	3,815	11.54%	3.82%
D	29,140	88.11%	29.14%

Extended Data Figure 9: Transcriptomic profiling of LS *Crhr2* neuronal subclasses. **a**, Workflow schematic for single-nucleus RNA sequencing (snRNAseq) of GFP-positive nuclei isolated from *Crhr2*-Cre; Sun1-sfGFP mice, including cell isolation, GEM generation, barcoding, cDNA library preparation, and sequencing analysis. **b–d**, Fluorescence-activated cell sorting (FACS) gating strategy and cell identification, showing distinct cells (A–D) based on size and fluorescence intensity. **e**, Quantitative summary of sorted populations showing event counts and population percentages. **f**, Heatmap of gene expression profiles across identified neuronal clusters (0–9), illustrating distinct molecular signatures. **g**, Dot plot legend indicating fraction of cells expressing each gene and mean expression level. **h–r**, Dot plots illustrating differential gene expression across clusters for key functional gene families: (**h**) fast neurotransmitters, (**i**) glutamate receptor subunits, (**j**) calcium signaling proteins, (**k**) opioid system components, (**l**) neuropeptides, (**m**) neuropeptide receptors, (**n**) dopamine receptors, (**o**) noradrenergic receptors, (**p**) serotonergic receptors, (**q**) cholinergic system components, and (**r**) hormone receptors.

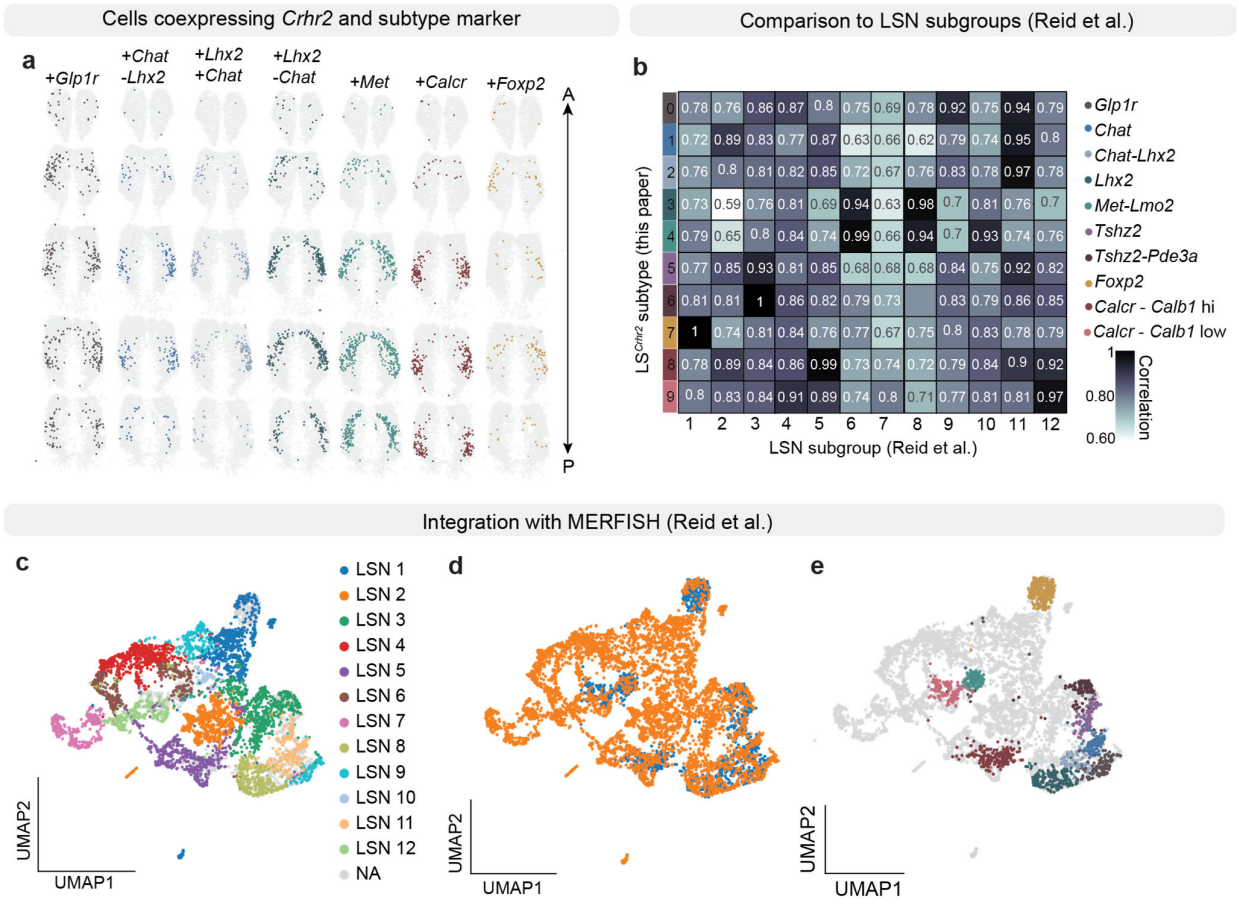

Extended Data Figure 10: Spatial and transcriptional alignment of LS *Crhr2* neuronal subclasses with previously identified LSN subgroups. a, Spatial mapping of cells co-expressing *Crhr2* and molecular subtype markers (Glp1r, Chat, Lhx2, Met, Calcr, Foxp2), illustrating distinct anatomical distributions. **b**, Correlation matrix comparing molecularly defined LS^{Crhr2} subtypes from this study (rows) to previously identified lateral septum neuronal (LSN) subgroups from Reid et al. (columns), demonstrating significant similarity in their transcriptional identifiers. **c–e**, Integration of snRNAseq data from this study with spatially resolved MERFISH data from Reid et al.: (**c**) UMAP visualization showing original LSN subgroup identities, (**d**) overlay of Crhr2-expressing cells from this study (blue) onto MERFISH-based UMAP (orange), and (**e**) visualization of the transcriptionally defined LS^{Crhr2} subtypes (color-coded) integrated with MERFISH spatial data (gray).

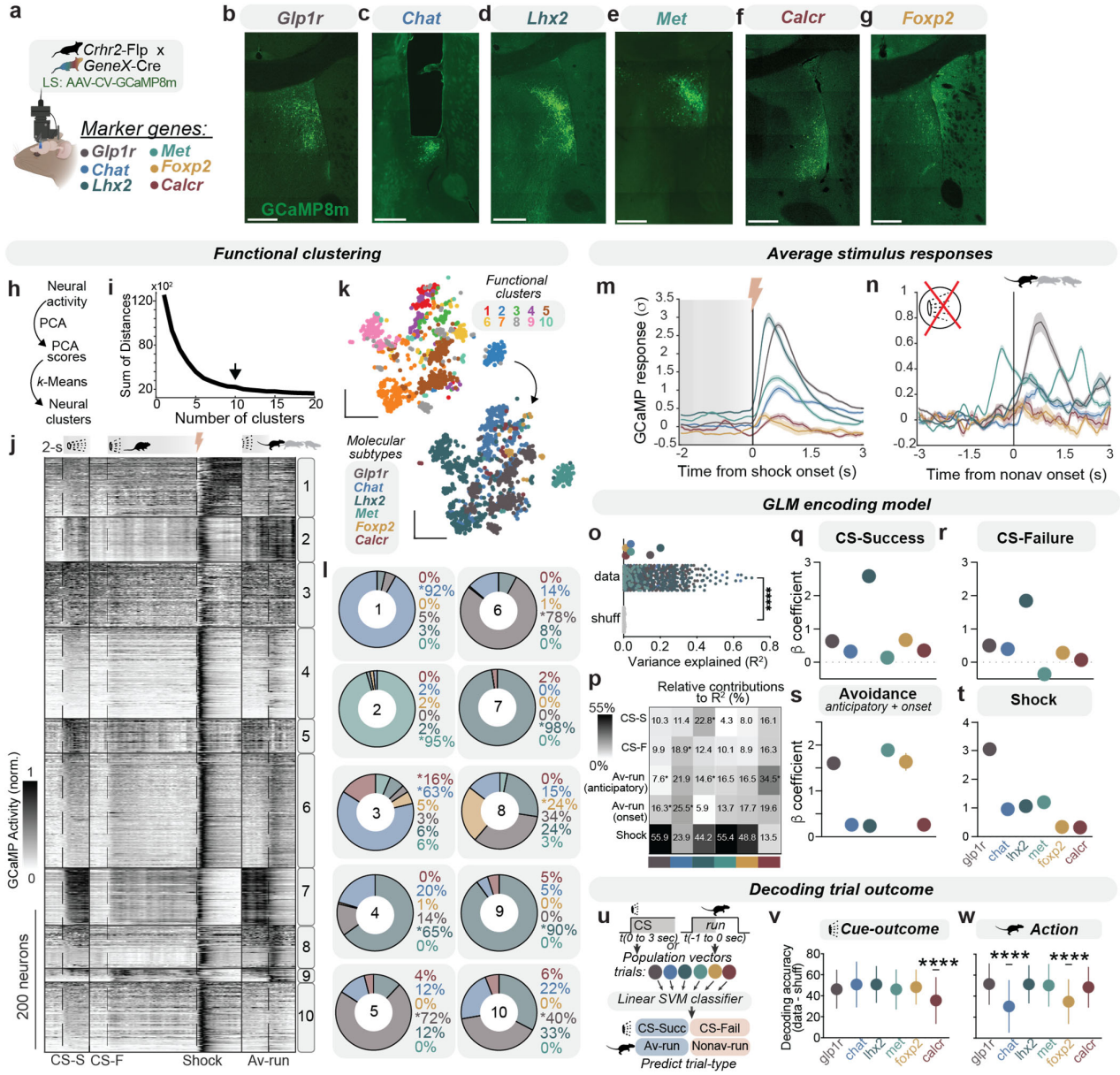

Extended Data Figure 11: Functional clustering and GLM analysis of molecularly defined LS *Crhr2* neuronal subclasses. **a**, Schematic illustrating the intersectional genetic approach for expressing GCaMP8m in molecular subtypes (*Glp1r, Chat, Lhx2, Met, Calcr, Foxp2*). **b–g**, Representative histological images showing selective GCaMP8m expression in molecular subtypes: (**b**) *Glp1r*, (**c**) *Chat*, (**d**) *Lhx2*, (**e**) *Met*, (**f**) *Calcr*, and (**g**) *Foxp2*. Scale bars, 500 um. **h**, Workflow schematic for functional clustering based on PCA scores from neural activity data. i, Elbow plot for k-means clustering analysis, indicating the optimal number of functional clusters (arrow). **j**, Heatmap of neuronal activity aligned to CS-success (CS-S), CS-failure (CS-F), shock, and avoidance run (Av-run) events. Clusters labeled 1–10, n = [1] 86, [2] 65, [3] 94, [4] 132, [5] 50, [6] 167, [7] 83, [8] 62, [9] 20, [10] 101 neurons).. **k**, UMAP plots illustrating clustering of neurons by functional activity (top), color-coded by molecular subtype (bottom), illustrating that activity-dynamics largely map onto molecular identiy. **l,** pie charts indicate molecular subtype composition within each functional cluster. Asterisks or each color coded percentage represents a significant increase above chance in the proportional representation of that molecular type within cluster (permutation test). **m–n**, Average calcium responses across molecular subtypes to (**m**) shock onset and (**n**) non-avoidance (nonav) onset. **o**, GLM variance explained (R^2) for real versus shuffled data, highlighting significant predictive accuracy of the model, color coded by subtype. **p,** Heatmap displaying relative contribution of each variable to the total variance explained by the GLM encoding model. Average relative contributions for each subtype are shown. Asterisks indicate significantly different relative contributions (ANOVA, Bonferroni post-hoc test). **q–t**, GLM-derived β coefficients representing differential responses across subtypes to (**q**) CS-success, (**r**) CS-failure, (**s**) combined avoidance (anticipatory and onset), and (**t**) shock. **u**, Schematic of linear SVM decoding strategy predicting trial outcomes based on subtype-specific neuronal activity. **v–w**, Decoding accuracy illustrating differential contributions of subtypes in predicting (**v**) cue-outcome outcomes and (**w**) action-related outcomes (mean ± SEM; ANOVA). The Calcr-expressing subset online performs worse than all other subtypes when using Cue onset signals, while both Chat and Foxp2 subsets perform worse than others when using prior-to-action signals. *P < 0.05, **P < 0.01, ***P < 0.001,****P < 0.0001.

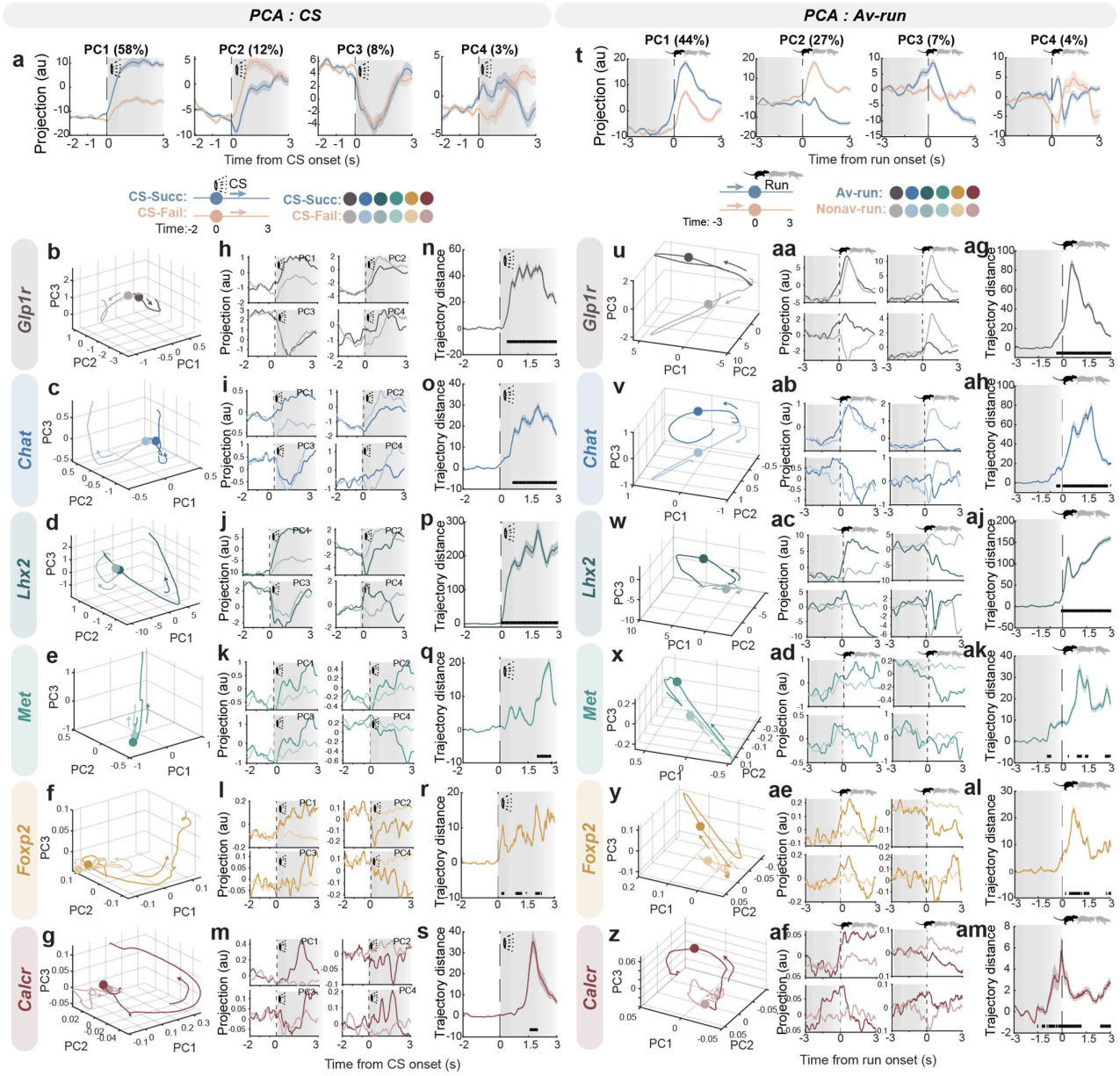

Extended Data Figure 12: PCA reveals distinct neural trajectories and dynamics across molecularly defined LS *Crhr2* subtypes. **a**, Neural trajectories fit to principal components (PC1–4) aligned to CS onset, illustrating differential temporal dynamics during success (CS-Succ; blue) and failure (CS-Fail; orange) trials. **b–g**, 3D PCA trajectory plots (left) and corresponding temporal activity projections (right) for molecular subtypes (**b**) Glp1r, (**c**) Chat, (**d**) Lhx2, (**e**) Met, (**f**) Foxp2, and (**g**) Calcr, showing subtype-specific neural responses during CS-Succ (blue) and CS-Fail (orange) pseudopopulation trials. Circles represent CS onset. **h–s**, Temporal dynamics of neural trajectories from CS onset for each subtype (**h-m**), quantifying trajectory distances and divergence patterns (**n–s**). Thick black lines signify significance (permutation test, p<0.05, See *Methods*). **u–z**, 3D PCA trajectory plots (left) and corresponding temporal activity projections (right) for molecular subtypes (**u**) Glp1r, (**v**) Chat, (**w**) Lhx2, (**x**) Met, (**y**) Foxp2, and (**z**) Calcr, showing subtype-specific neural responses during Av-run (blue) and Nonav-run (orange) pseudopopulation trials. Circles represent Run onset. **aa-am**, Temporal dynamics of neural trajectories from Run onset for each subtype (**aa-af**), quantifying trajectory distances and divergence patterns (**ag-am**). Thick black lines signify significance (permutation test, p<0.05, See *Methods*).

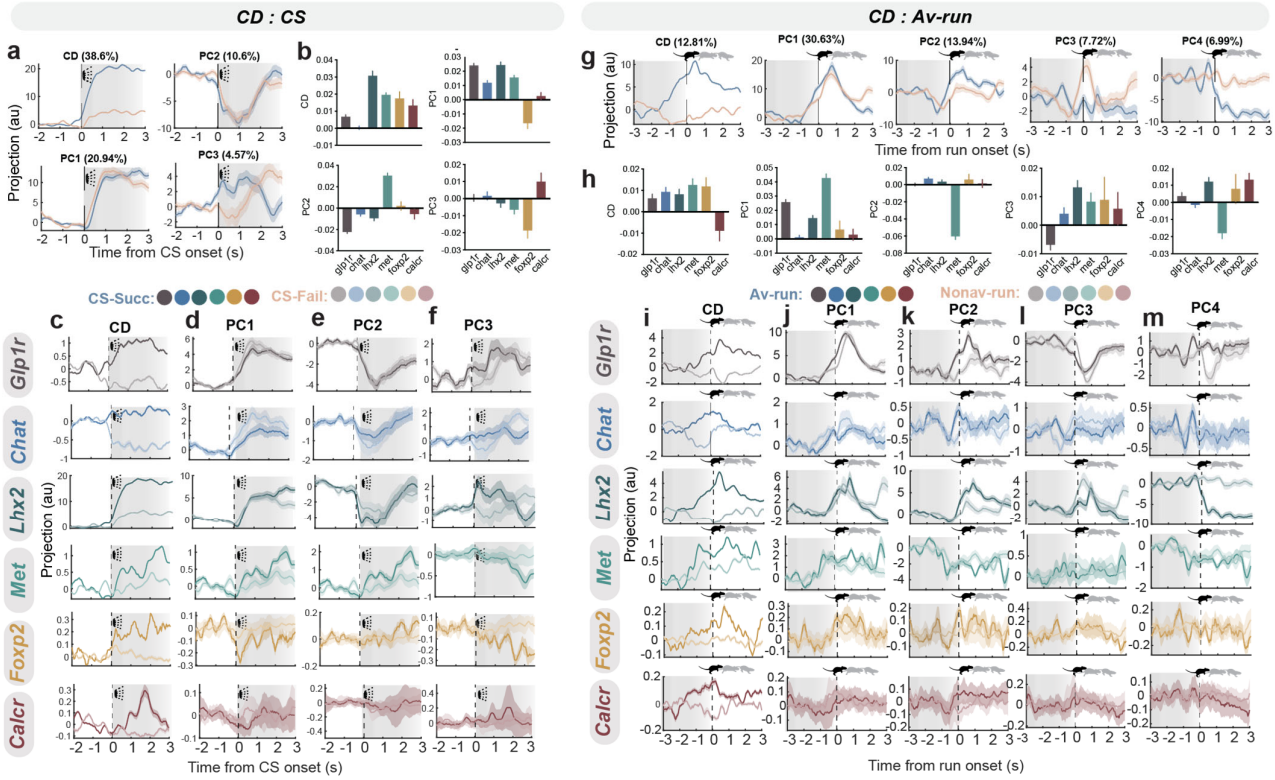

Extended Data Figure 13: Coding direction (CD) and PCA differentiate molecular subtype dynamics during cue and av-run epochs. **a**, Temporal dynamics of CD and principal components (PC1–PC3) aligned to conditioned stimulus (CS) onset, highlighting differential neural responses for success (CS-Succ) and failure (CS-Fail) trials. **b**, Coefficients for each CD and PC (mean ± SEM) across subtypes, illustrating differential contribution by each subtype across dimensions for the CS alignment. **c–f**, Neural trajectories aligned to CS onset fit to the neural activity of each molecular subtype, depicting specific temporal activity patterns across CD (**c**) and PCs 1–3 (**d–f**) for each subtype (top to bottom: Glp1r, Chat, Lhx2, Met, Foxp2, Calcr). **g**, Temporal dynamics of CD and principal components (PC1–PC3) aligned to run onset, highlighting differential neural responses for Av-run and Nonav-run trials. **h**, Coefficients for each CD and PC (mean ± SEM) across subtypes, illustrating differential contribution by each subtype across dimensions for the Run alignment. **i-m,** Neural trajectories aligned to run onset fit to the neural activity of each molecular subtype, depicting specific temporal activity patterns across CD (**i**) and PCs 1–3 (**j-m**) for each subtype (top to bottom: Glp1r, Chat, Lhx2, Met, Foxp2, Calcr).

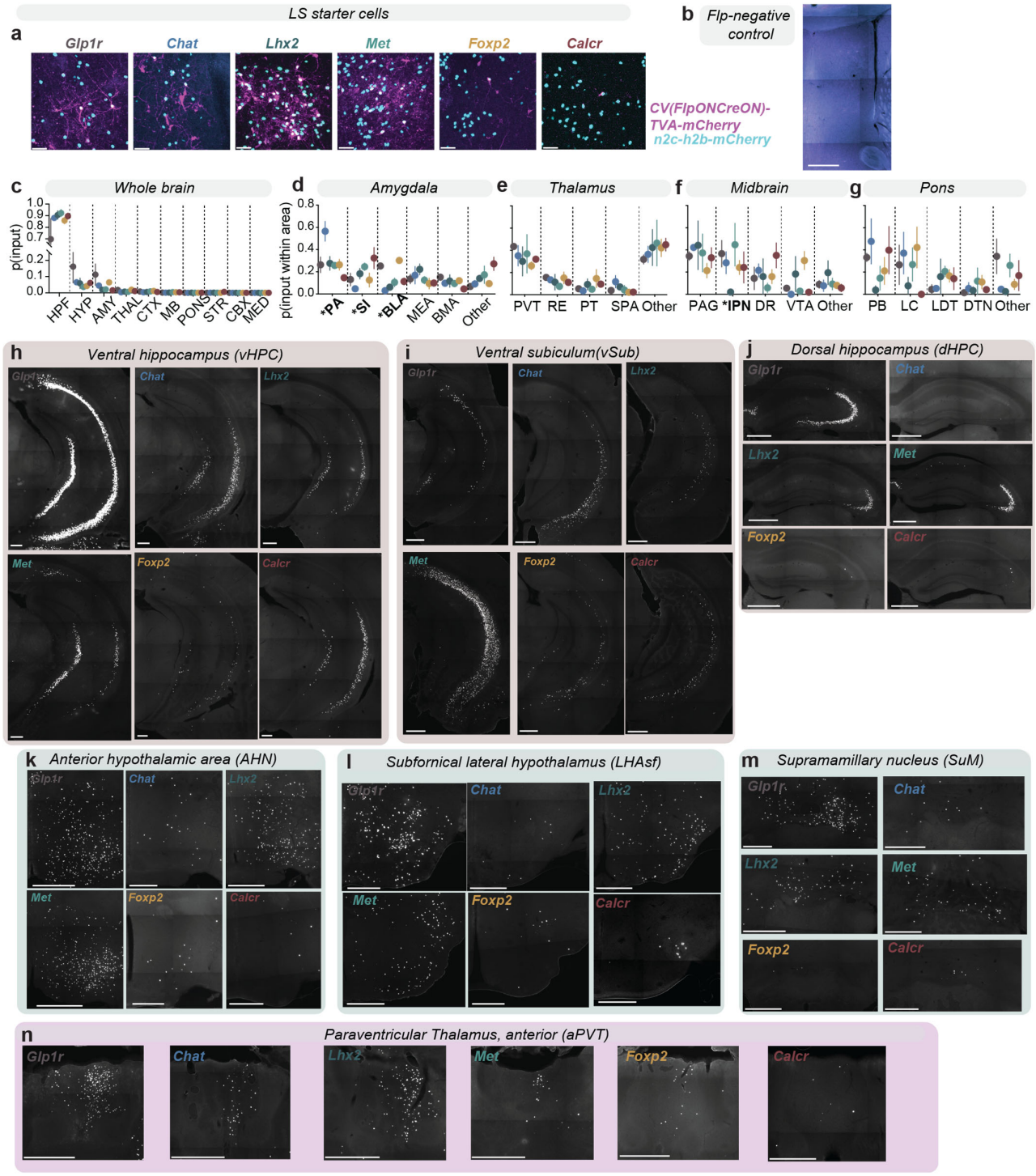

Extended Data Figure 14: Anatomical characterization of monosynaptic inputs to molecularly defined LS Crhr2 neuronal subclasses. **a**, Representative images of LS starter cells for each molecular subtype (Glp1r, Chat, Lhx2, Met, Foxp2, Calcr), demonstrating successful rabies-assisted labeling. Scale bars, 100um. **b**, Control image confirming absence of intersectional labeling in Flp-negative conditions. Scale bar, 500um. **c–g**, Quantitative summary of whole-brain input distributions (fraction of total inputs; **c**) and detailed breakdown of inputs from specific brain areas: (**d**) amygdala, (**e**) thalamus, (**f**) midbrain, and (**g**) pons (mean ± SEM). One-way ANOVA, *P<0.05. **h–j**, Representative histological images showing subtype-specific input distributions within the hippocampal formation, including (**h**) ventral hippocampus (vHPC), (**i**) ventral subiculum (vSub), and (**j**) dorsal hippocampus (dHPC). Scale bars, 500um. **k–m**, Representative images illustrating hypothalamic input specificity for each subtype from (**k**) anterior hypothalamic area (AHN), (**l**) subfornical lateral hypothalamus (LHAsf), and (**m**) supramamillary nucleus (SuM). Scale bars,500um. **n**, Representative images of subtype-specific inputs from the anterior paraventricular thalamus (aPVT). Scale bars, 500um.

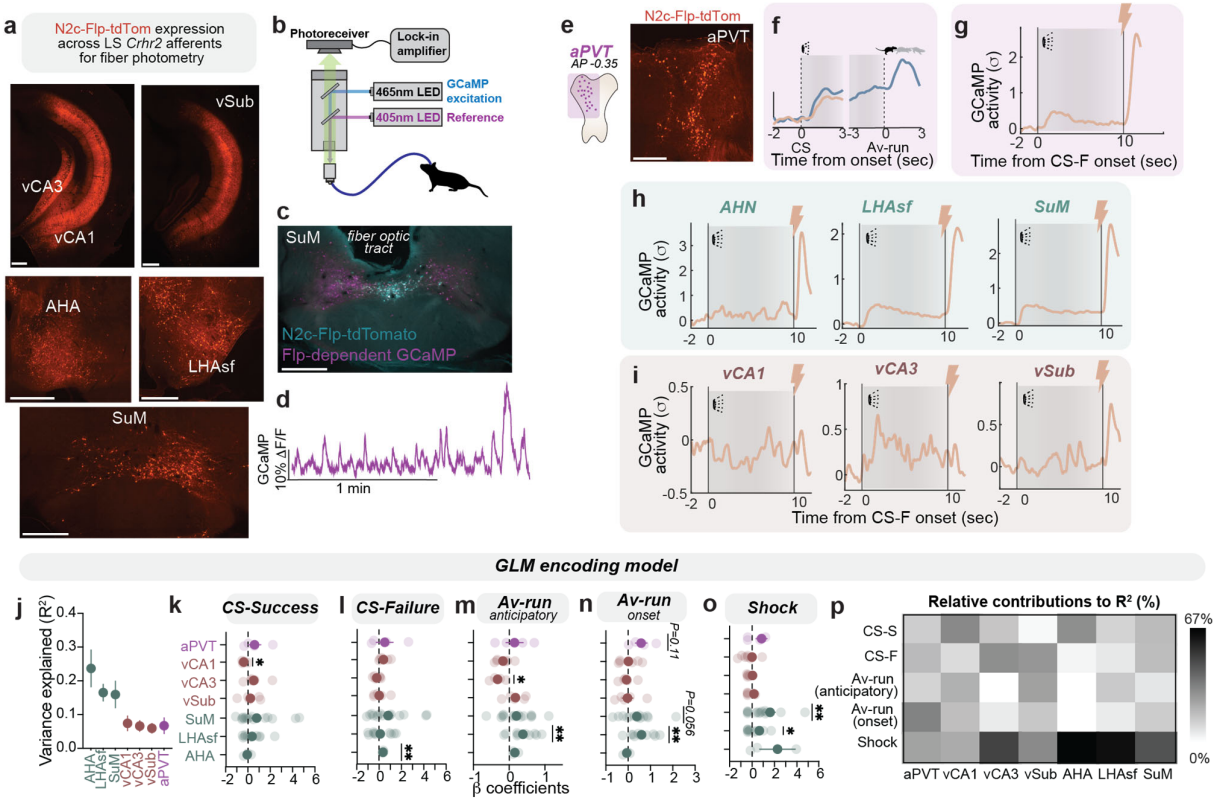

Extended Data Figure 15: Functional validation fiber photometry recordings of afferents from the hippocampus, hypothalamus, and thalamus during active avoidance and GLM analysis. **a**, Representative expression of Flp-tdTomato in hippocampal (vCA1, vCA3, vSub) and hypothalamic (AHA, LHAsf, SuM) afferents following CVS-N2cΔG-Flp-tdTomato rabies virus injection into LS of *Crhr2*-Cre mice. Scale bar, 500um. **b**, Schematic illustrating the fiber photometry approach for recording calcium dynamics. **c**, Representative image of GCaMP expression and optical fiber placement in the SuM. Scale bar, 500um.**d**, Example calcium transient from hypothalamic SuM afferents recorded via fiber photometry. **e–g**, Representative image (**e,** Scale bar, 500um) and average calcium activity responses (**f–g**) to CS and shock events in anterior paraventricular thalamus (aPVT), n= 4 mice**. h–i**, Average calcium activity aligned to CS-Fail trials and shock across (**h**) hypothalamic (AHN, LHAsf, SuM) and (**i**) hippocampal (vCA1, vCA3, vSub) afferents. **j–o**, GLM analysis quantifying variance explained (R^2, **j**) and β coefficients for responses to (**k**) CS-Success, (**l**) CS-Failure, (**m**) anticipatory Av-run, (**n**) Av-run onset, and (**o**) shock across afferent regions. One sample t-tests. **p**, Heatmap depicting relative contributions to explained variance (R^2) from behavioral events across afferent inputs, depicting stronger contributions of specific variables depending on subtype. For example, aPVT to Av-run onset, vCA1 to CS-S, vCA3 to CS-F and shock, AHA to CS-S and shock, LHAsf to anticipatory Av-run and shock, and SuM to both CS and shock. vCA1, n= 7 mice; vCA3, n= 5 mice; vSub, n= 5 mice; AHN, n= 3 mice; LHAsf, n= 10 mice; and SuM, n= 15 mice. **P* < 0.05, **P < 0.01, ***P < 0.001,****P < 0.0001.